2024 23rd IEEE Intersociety Conference on Thermal and Thermomechanical Phenomena in Electronic Systems (ITherm) | 979-8-3503-6433-0/24/$31.00 ©2024 IEEE | DOI: 10.1109/ITherm55375.2024.10709510

Unveiling the Dual Limits of Critical Heat Flux and Implications for Immersion Cooling

Suhas Tamvada[1], Daniel Attinger[2], and Saeed Moghaddam[1,*]
[1] *Department of Mechanical and Aerospace Engineering*, *University of Florida, Gainesville, FL, USA*
[2] *Struo LLC, Ames, Iowa, USA*
* Corresponding author: saeedmog@ufl.edu

***Abstract*— Rising electronics power density has led to the adoption of immersion cooling as a thermal management strategy for next generation chips. However, immersion cooling is plagued by the critical heat flux (CHF) limit, which dictates the maximum heat transfer from a surface. Following its discovery in 1934 by Nukiyama, two explanations, namely the hydrodynamic instability theory introduced by Kutateladze in 1948 and established by Zuber in 1959, and the evaporation momentum theory conceptualized by Steinchen and Sefiane in 1996 and formalized by Kandlikar in 2001, have hitherto predicted a similar CHF limit (~ 100 W/cm^2 for water on a copper surface) despite hinging on contrasting physical phenomena. Here, we show through rigorous experimental and analytical investigation of boiling using liquids with diverse thermophysical properties and planar heater surfaces representing 44 unique experimental conditions, that the critical heat flux limit due to evaporation momentum (CHF_{EM}) is approximately four times higher than the hydrodynamic instability limit (CHF_{HI}) predicted by Zuber. Remarkably, this elevated CHF_{EM} becomes manifest only when the hydrodynamics of liquid and vapor flow above the heater surface are fully stabilized. Our experiments demonstrate the existence of these two asymptotic limits governed by hydrodynamic and surface limitations, respectively, depending on hydrodynamic flow conditions above the heater surface such that the ratio CHF/CHF_{EM} ranges from 0.2 to 1 across all examined fluids. Evaporation momentum theory encompasses the force balance on a bubble, which is evidenced in our experiments showing the presence of nucleating bubbles even as the surface heat flux approaches CHF. Further, a theoretical model is developed to predict CHF based on the single bubble assumption, and closely matches experimental data. Unlike previous assumptions, we find that the effect of gravity is negligible. This work could provide guidelines for development of surface topologies suitable for immersion cooling.**

Keywords—boiling, critical heat flux, evaporation momentum, hydrodynamic instability, immersion cooling, electronics cooling

I. Introduction

As modern electronics and high-power lasers continue to evolve in complexity and performance, their thermal management emerges as a critical challenge, requiring reliable cooling solutions capable of maintaining low junction temperatures [1]. Thermal management is an essential element of data centers technology, contributing to substantial energy consumption hence requiring advancements in heat removal strategies to ensure energy efficiency [2], [3]. To tackle this growing need, phase-change immersion cooling is emerging as an alternative thermal management strategy owing to its capability to remove large amounts of heat while maintaining the chip isothermal [4], [5]. Phase-change immersion cooling relies on boiling of the coolant to remove heat from the chips [6]. To benefit from two-phase immersion cooling, the design of boiling surfaces and liquid coolants must be informed by the fundamentals of pool boiling heat transfer [7]. A long-standing question in this regard has revolved around the underlying physics of the upper limit of nucleate boiling heat transfer, commonly known as the critical heat flux (CHF). At CHF, the rate of vapor formation at the boiling surface increases to a degree that prevents returning liquid from rewetting the heater. The formation of a resulting vapor blanket on the heater surface triggers a rapid, often catastrophic, rise in the heater temperature leading to burnout and failure of electronics. An unclear understanding of this limit leads to the operation of many such thermal systems below their potential. To advance immersion cooling, the limits of CHF must be established unequivocally.

CHF was initially discovered by Nukiyama in the year 1934 [8]. Subsequent research spanning nearly a century has been dedicated to elucidating the physics underlying this phenomenon and advancing the CHF threshold. Numerous studies have been undertaken to investigate the influence of various factors on CHF such as liquid properties [9], [10], surface wettability [11], [12], surface capillary wicking [13], [14], surface roughness [15], heater size [16], and component orientation [17], [18]. The predominant theoretical framework explaining CHF has been the hydrodynamic theory, initially postulated by Kutateladze [19], and further refined into a mathematical model by Zuber in 1958 [20]. This theory correlates CHF with the instability phenomena occurring in the liquid and vapor columns above a heated surface. The hydrodynamic model remained the leading theory for approximately four decades [21]. A new perspective was offered in 1996 by Steinchen and Sefiane [22], who explored the hypothesis that a boiling crisis could be initiated by rapid vapor recoil forces at the liquid-solid interface, leading to the formation of the evaporation momentum theory. Building on these principles, Kandlikar formulated an empirical correlation that incorporates the effects of the liquid-surface contact angle and heater orientation, based on the evaporation momentum force theory [23].

This work is supported by the National Science Foundation grant number CBET1934354

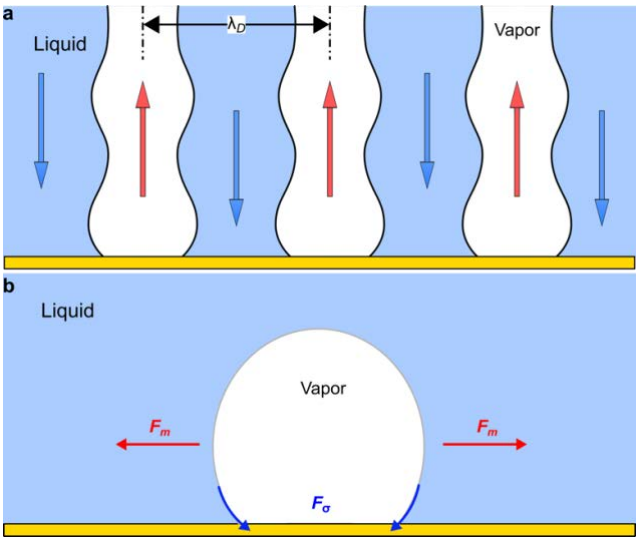

Fig. 1. (**a**) Hydrodynamic theory postulates that the interaction of escaping vapor (denoted by red arrows) and returning liquid (denoted by blue arrows) columns away from the surface trigger CHF when the distance between the vapor columns reaches a critical value (λ_D) based on Taylor instability [24]. (**b**) A vapor pocket growing on a hot surface is subject to a momentum force $\boldsymbol{F_m}$ (direction of force shown by red arrows) which tries to expand the pocket radially outwards, and the surface tension force $\boldsymbol{F_\sigma}$ (shown by the blue arrows) acting along the periphery of the vapor pocket which work to retain the shape of the bubbles and pin the vapor pocket to the surface. Evaporation momentum theory states that CHF is triggered when the evaporation momentum force outweighs the restoring forces.

Figs. 1(a) and (b) illustrate two leading theories explaining CHF phenomena. Zuber's hydrodynamic theory [20] suggests that increasing heat flux intensifies bubble formation, leading to the formation of vapor columns (Fig. 1(a)). These columns obstruct liquid return to the surface as their velocity surpasses a critical point, causing liquid-vapor interface destabilization—a process akin to Taylor [24] and Helmholtz [25] instabilities—at a critical spacing (λ_D). Hence, CHF results from hydrodynamic instabilities above the heater-liquid interface. While widely used for CHF prediction, this model does not incorporate the effect of surface geometry and wetting properties [26]. Conversely, the evaporation momentum theory attributes CHF to a force imbalance at the heater's three-phase contact line. Kandlikar's model [23] indicates that CHF arises from momentum due to rapid evaporation at dry spots (see Fig. 1(b)). This momentum creates a lateral force (red arrows), expanding the dry patch by pushing liquid outwards, counteracted by surface tension and vapor buoyancy. CHF occurs when evaporation momentum overpowers these forces, causing the vapor pocket to expand swiftly. Both hydrodynamic and evaporation momentum theories predict similar CHF values (~110 W/cm^2 for water on smooth copper at 1 atm) and fail to account for higher experimental CHF values. In this work, we establish the conditions for observing the hydrodynamic (CHF_{HI}) and evaporation momentum (CHF_{EM}) limits through experiments and theoretical analysis, challenging the premise that they can be co-limiting under identical conditions [27]. Furthermore, gravitational aspects of the evaporation momentum model which were hitherto unreported are discussed along with a visual analysis of boiling close to CHF. In subsequent sections, it will be shown that when hydrodynamic flow is ordered adequately, bubble nucleation can be observed very close to CHF. Lastly, implications for immersion cooling will be discussed, showing that through progressive ordering of liquid-vapor flow, chip isotherms can be maintained for a wide range of heat fluxes.

II. Experiment

A. Test Liquids

To understand CHF limits in the context of immersion cooling, we test three different liquids with widely different thermophysical properties: namely water, ethanol, and n-perfluorohexane (3M Fluorinert FC-72©). Water is chosen as it is a key reference fluid involved in numerous past studies. Ethanol is used as another reference fluid with a surface tension in between that of water and FC-72. FC-72 is a dielectric coolant with a boiling point of 56 ℃ at atmospheric conditions chosen as a representative of low-pressure inert fluids used for immersion cooling. Table I shows properties of the 3 liquids at 25℃ and 1 atm (101.325 kPa).

TABLE I. Liquid properties at 25 ℃ and 1 atm

Liquid	Liquid density P_l (kg/m^3)	Vapor density ρ_v (kg/m^3)	Surface tension σ (N/m)	Heat of vaporization h_{fg} (kJ/kg)
Water	998	0.59	0.072	2256.4
Ethanol	789	1.59	0.022	918.16
FC-72	1680	13.13	0.010	88

B. Test Device

Fig. 2 illustrates the experimental setup, featuring a furnace set into a PTFE block with two 315 W cartridge heaters. We integrated copper fins with dimensions—20 mm height, 10 mm length (L), and varying widths (W) of 10, 2, 1, and 0.5 mm—using a high-temperature solder (Pb93.5Sn5Ag1.5) to obtain four distinct test surfaces. 'T' type thermocouples, with a solder thermal conductivity of 60 W/m-K, were embedded into micro-posts on the fin's side to record the temperature profile, placing the uppermost sensor (T_1) 0.5 mm from the top to gauge the fin's temperature gradient (see Fig. 2). The fins were insulated using polydimethylsiloxane (PDMS) whose thermal conductivity (k_{PMDS} = 0.15 W/m-K) is ≈2500 times lower than that of copper (k_{Cu} = 398 W/m-K) to minimize heat loss. Heat flux between 2 consecutive thermocouples is calculated using Fourier's law ($q'' = -k_{Cu}(\Delta T/\Delta x)$), where ΔT is the temperature difference between the two thermocouples, and Δx (4 mm) is the spacing between them. Surface temperatures (T_s) were estimated by extrapolating thermocouples measurements, and the average of 3 heat fluxes is reported.

To maintain consistent surface properties across all tests, all surfaces were cleaned with acetone, ethanol, isopropyl alcohol, and deionized water, and consecutively smoothed with sandpapers of 1500 grit and 3000 grit. Next, they were polished using MAAS metal polish to remove any inherent oxide layer and reduce surface roughness. Static liquid contact angles of

60±2, 12±2, and 4±1 for water, ethanol, and FC-72, respectively were recorded prior to experiments.

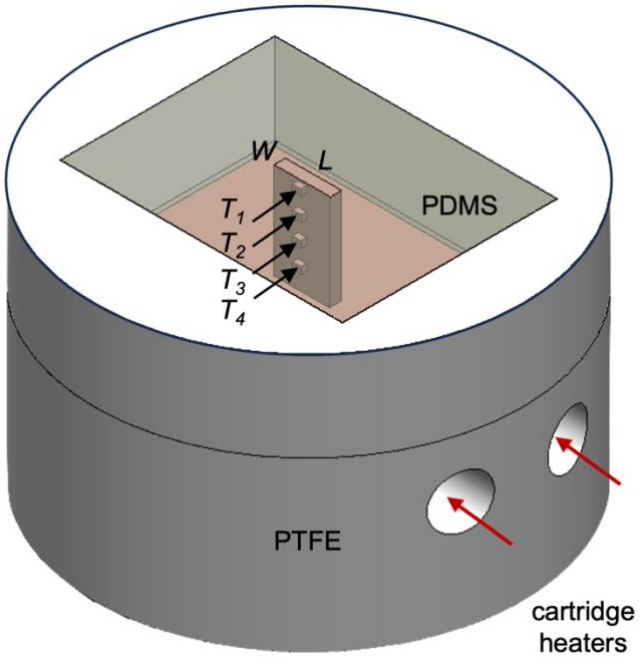

Fig. 2. Test device consisting of copper heater block, PTFE and PDMS insulation. Cartridge heaters of 315 W each are inserted into the holes indicated by red arrows. Four T type thermocopuples are embedded to record temperature. The length (L) of the copper fin is 10 mm, while the width (W) is altered between 10, 2, 1, and 0.5 mm to obtain 4 test surfaces.

C. Experiment Setup

Fig. 3 presents a schematic of our experimental setup within an 8×8×8 inch vacuum chamber, featuring quartz glass walls for observation. The setup includes 2 light sources, 2 diffuser plates, and a power supply to power the cartridge heaters through a power inlet feedthrough (indicated in red).

Two 500 W auxiliary heaters regulated the working fluid's temperature and chamber pressure. A fifth 'T' type thermocouple monitored the fluid's saturation temperature (T_{sat}). An Agilent DAQ (34970A) recorded temperature and pressure data. Two high-speed cameras (Photron FASTCAM SA4) were operated synchronously in orthogonal directions to capture the physics close to the surface. The recording of the boiling process close to the surface provide conclusive details about bubble formation close to CHF which were hitherto debated in literature.

D. Experimental Procedure

Each experiment was set up by placing the heater device inside the chamber, charging the working liquid, and degassing the liquid by vacuuming the chamber for 3 to 4 hours. The chamber pressure and correspondingly saturation temperature were controlled using auxiliary heaters such that the liquid followed its saturation pressure curve. The heaters were supplied with AC power to increase heat flux in increments of 10 W/cm^2 after temperatures reached a steady state. At a certain point in the experiment, the temperatures rise rapidly indicating CHF. At this point, the experiment is stopped. This is illustrated in Fig. 4 which shows temperature recordings from the DAQ during an experiment.

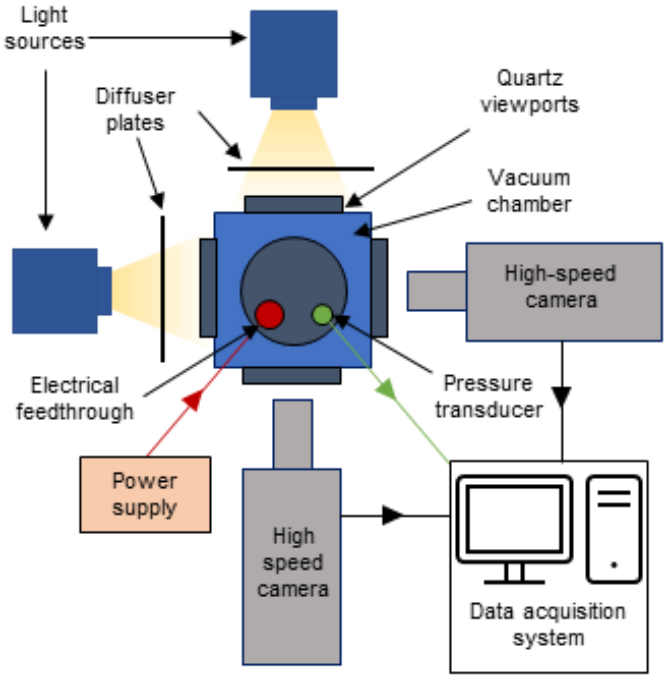

Fig. 3. Experimental test loop consisting of a vacuum chamber, 2 LED illuminators, 2 diffuser plates, 2 high speed cameras, a power supply, and data acquisition (DAQ) system. The vacuum chamber contains an electrical feedthrough for routing of wires. A pressure transducer is placed on the vacuum chamber to record pressure inside the chamber.

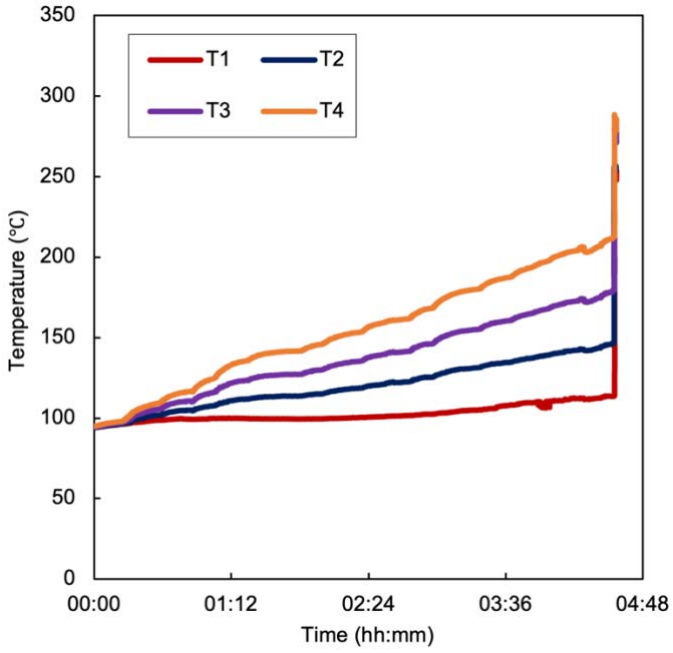

Fig. 4. Sample experimental run showing temperature data from 4 thermocouples as a function of time. The sudden uptick in temperatures signify CHF and the end of an experiment.

To maintain constant saturation conditions inside the chamber during an experiment, heat loss from the chamber to the surroundings was considered. The pressure and temperature

inside the chamber is maintained through a balance between the power supplied to the main and auxiliary heaters, as well as the heat loss from the chamber to surroundings. Fig. 5 shows the pressure inside the chamber over the course of an experiment conducted at 101 kPa, illustrating constant saturation conditions.

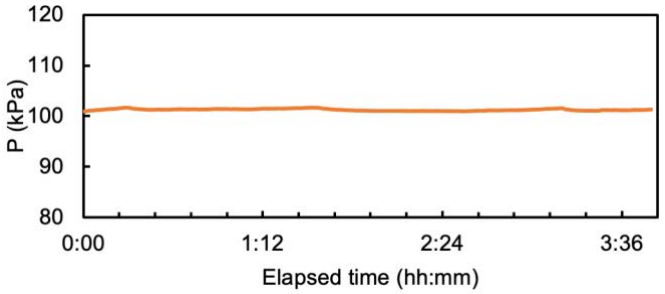

Fig. 5. Pressure inside the chamber as a function of elapsed experiment time for an experiment conducted at 101 kPa. The pressure is maintained constant during the entire duration of the experiment.

E. Data Reduction

Temperature readings from tests conducted at 4 different pressures (16.6, 33.3, 66.7, 101.3 kPa) were reduced to heat fluxes as described in section II (B), and the maximum heat fluxes recorded at CHF are reported.

High-speed videos are analyzed using ImageJ, an open-source image processing software. The images were analyzed to characterize the progression of boiling and determine dynamic contact angles of the liquid near CHF.

F. Uncertainty and Error Analysis

The uncertainty in heat flux is caused by uncertainty in temperature readings, thermal conductivity of copper, and spacing between the thermocouples. Equation (1) was used to calculate the uncertainty in heat flux

$$\frac{\delta q''}{q''} = \left[\left(\frac{\delta k}{k}\right)^2 + \left(\frac{\delta \Delta T}{\Delta T}\right)^2 + \left(\frac{\delta \Delta x}{\Delta x}\right)^2\right]^{(1/2)} \quad (1)$$

where δk , $\delta \Delta T$, $\delta \Delta x$ are the uncertainties in thermal conductivity, temperature gradient, and distance between thermocouples, respectively. Since the surface heat flux is the average of the three heat fluxes, the temperature difference is calculated as $\Delta T = (T_1 + T_2 + T_3 + T_4)/4$. Hence, $\delta \Delta T$ can be calculated using (2).

$$\delta \Delta T = [(\delta T)^2 + (\delta T)^2 + (\delta T)^2 + (\delta T)^2\,]^{\left(\frac{1}{2}\right)} \sim 2\delta T \quad (2)$$

The uncertainty in different experimental variables are tabulated in Table II.

TABLE II. UNCERTAINTIES OF MEASURED VARIABLES

Variable	Uncertainty
δT	±0.5 K
$\delta k/k$	±2%
$\delta \Delta x/\Delta x$	±0.3%
$\delta A/A$	0.2%
$\delta P/P$	±0.25%

The uncertainty in heat flux is found to be ±20.2% at a lower value of 14 W/cm^2 and ±3.1% at the highest value of 370 W/cm^2. Additionally, we ensured that there is no heat loss in the fin section by calculating the heat fluxes between consecutive thermocouples and comparing them against the average heat flux from the three measurements in Fig. 6. The individual heat fluxes do not show any appreciable difference, confirming that the heat loss is negligible across the fin.

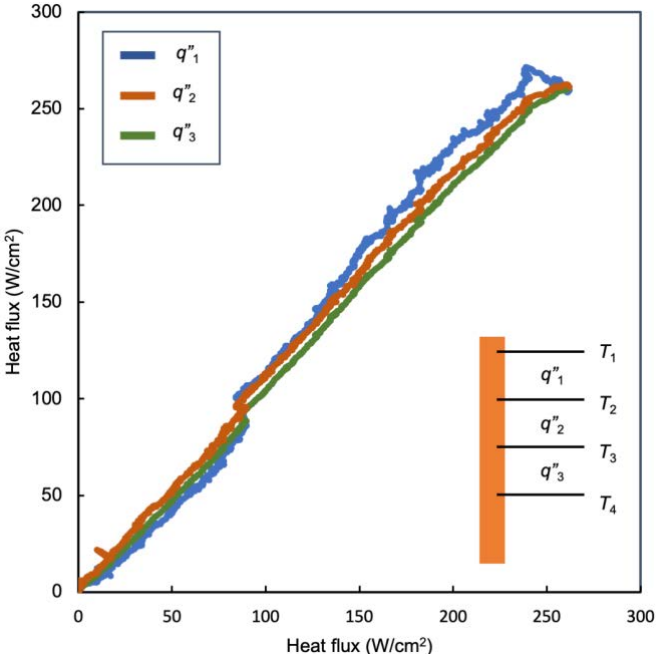

Fig. 6. Individual heat fluxes between consecituve thermocouples as a function of the average heat flux for an experiment conducted with water at 66 kPa. No significant difference is observed among the individual heat fluxes, indicating negligible heat loss across the fin section.

III. RESULTS AND DISCUSSION

A. Experimental Observations

The progression towards CHF is similar on all heaters and a detailed visual analysis is presented in [27]. Initially, as the surface is heated, surface temperatures rise, eventually resulting in nucleation of bubbles, initiating boiling. An increase in heat flux is visually indicated by an increase in frequency of bubble generation in the nucleate boiling regime [28]. At higher heat fluxes, bubbles coalesce close to the surface to form large vapor pockets. On large heaters (W = 10 mm), this phenomenon typically leads to dry patches which keep growing in size [28]. At extremely high heat fluxes, the entire surface is engulfed by vapor, indicating CHF. On the smaller heaters (W = 2, 1, 0.5 mm), the boiling process follows a similar pattern in the nucleate boiling regime. However, since the smaller heaters allow enhanced liquid replenishment along their length, the formation of dry patches is negligible. In fact, a widely debated idea in literature has been the nature of vapor formation on a surface close to CHF. Many studies have reported that close to CHF, the surface experiences partial dryout with hot spots on the surface [28]. Others have hypothesized a thin liquid microlayer supplied liquid to the surface even close to CHF. Our experiments on

hydrodynamically enhanced boiling conditions shows the nucleation of bubbles close to CHF. This is illustrated in Fig. 7 which shows a snapshot of FC-72 boiling on a 1 mm surface at a heat flux of ~ 35 W/cm^2, which is greater than twice the Zuber limit.

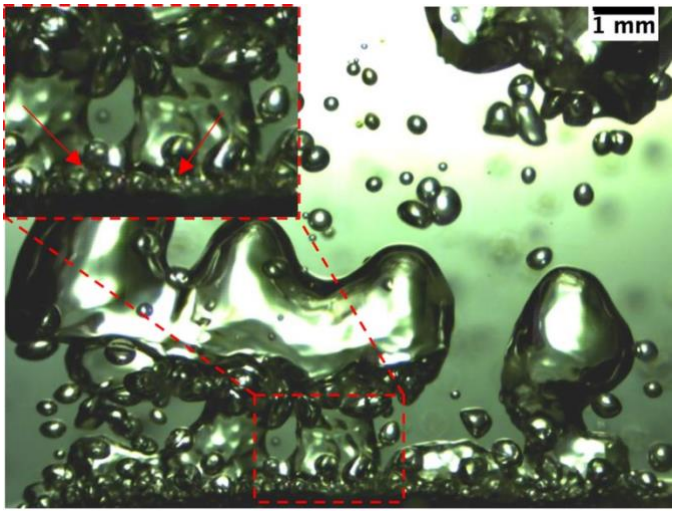

Fig. 7. FC-72 boiling on a 1 mm surface at ~ 35 W/cm^2. Enhanced liquid wetting due to hydrodynamic ordering leads to bubble nucleation even at high heat fluxes.

This phenomenon is attributed to enhanced liquid wetting even at high heat fluxes due to enhanced hydrodynamic ordering of the liquid and vapor. Coalescing vapor pockets on heaters with characteristic lengths exceeding the capillary length of the liquid lead to a marked CHF limit characterized by reduced heat flux and increased surface temperatures.

The image demonstrates that when hydrodynamic flow is ordered above the surface, heat flux can be significantly increased and the inhibition of vapor column coalescence leads to bubble formation on the surface due to efficient liquid rewetting. At higher heat fluxes, the contact line rapidly expands laterally, covering the heater and surrounding areas, signaling CHF (blue arrows). These findings are plotted in Fig. 8(a)-(c) against existing theoretical models.

Preliminary results indicate a decline in CHF values correlating with lower saturation pressures, aligning with established findings of boiling at diminished pressures [29]. Notably, there is a significant disparity in CHF values when comparing a large square heater to those under HEC conditions. The square heater, with a characteristic length surpassing the capillary length for all tested liquids, shows CHF constraints arising from hydrodynamic instabilities. This is corroborated by the pink curves representing Zuber's correlation [20], as outlined in (3)

$$CHF_{Zuber} = \frac{\pi}{24} h_{fg} {\rho_v}^{1/2} [\sigma g(\rho_l - \rho_v)]^{1/4} \qquad (3)$$

which considers the interaction of vapor columns away from the surface and does not account for the contact angle of the liquid. As heater sizes approach the liquid's capillary length, CHF notably increases due to the stabilization of above-surface liquid-vapor hydrodynamics. This is particularly evident with water (Fig. 8(a)), where heaters narrower than water's capillary length (2.73 mm) lead to substantially higher CHF values—up to four times Zuber's hydrodynamic limit at atmospheric pressure. For ethanol (Fig. 8(b)), a 2 mm heater width slightly enhances CHF due to improved hydrodynamic stability, and even more so when the heater width is below ethanol's capillary length. The trend is most pronounced for FC-72 (Fig. 8(c)), where CHF escalates consistently as flow hydrodynamics stabilize, peaking for heaters narrower than FC-72's capillary length (0.72 mm). The orange lines in Fig. 8, modeled to reflect the balance between evaporation momentum and surface tension, accurately forecast these CHF limits under stable conditions. These patterns suggest that by tailoring heater dimensions, flow hydrodynamics can be optimized, significantly enhancing fluxes where evaporation momentum becomes the dominant limitation, surpassing previous predictions [23].

While reducing heater dimensions below the liquid capillary length markedly raises CHF limits, a further decrease does not continue this trend. For water (Fig. 8(a)), CHF values reach a maximum and remain constant despite a heater width decrease to 0.5 mm, much less than its capillary length of 2.73 mm. Ethanol exhibits a similar trend (Fig. 8(b)), where CHF values stabilize when heater width narrows from 1 mm to 0.5 mm, suggesting a heat transport ceiling on smooth surfaces. Moreover, although the evaporation momentum force is a consistent factor, its interaction with multiple vapor columns on larger heaters leads to early film boiling transitions, below the potential CHF. By normalizing CHF against the experimental evaporation momentum limit (CHF_{EM}) and plotting it against the non-dimensionalized heater width (L_h/L_c), a clear demarcation between the hydrodynamically limited and evaporation momentum limited test cases is obtained. Here, L_c is the capillary length of the liquid, defined as $L_c = \sqrt{\sigma/(\rho_l - \rho_v)g}$, where g is the acceleration due to gravity (9.81 m/s^2), ρ_l is the liquid density, ρ_v is the vapor density, and σ is the interfacial tension between the liquid and vapor. The ratio L_h/L_c can also be interpreted through the square root of the Bond number, Bo = $(\rho g {L_h}^2)/\sigma$, which balances gravitational and capillary forces. Fig. 9 confirms that CHF exceeds Zuber's prediction and reaches the evaporation momentum threshold as heater size falls below the liquid's capillary length, a consistent result across various liquids, heater sizes, and pressures.

B. Theoretical Interpretation

To model CHF under conditions where liquid flow is hydrodynamically stable atop the surface, we turn to the evaporation momentum theory. Our analysis starts with a vapor pocket on a horizontal plane, as depicted in Fig. 10, idealized as a spherical cap to facilitate numerical analysis. This bubble comprises vapor of density ρ_v, encircled by a liquid of density ρ_l, with a bubble radius of r_b and a contact radius on the surface r_c. The liquid-vapor interfacial tension is represented by σ, the liquid contact angle by β, and g stands for gravitational acceleration. The sphere's geometric center is the origin O', with points on the sphere described by radial (r), azimuthal (θ), and polar (φ) coordinates in the spherical system, while x, y, z denote

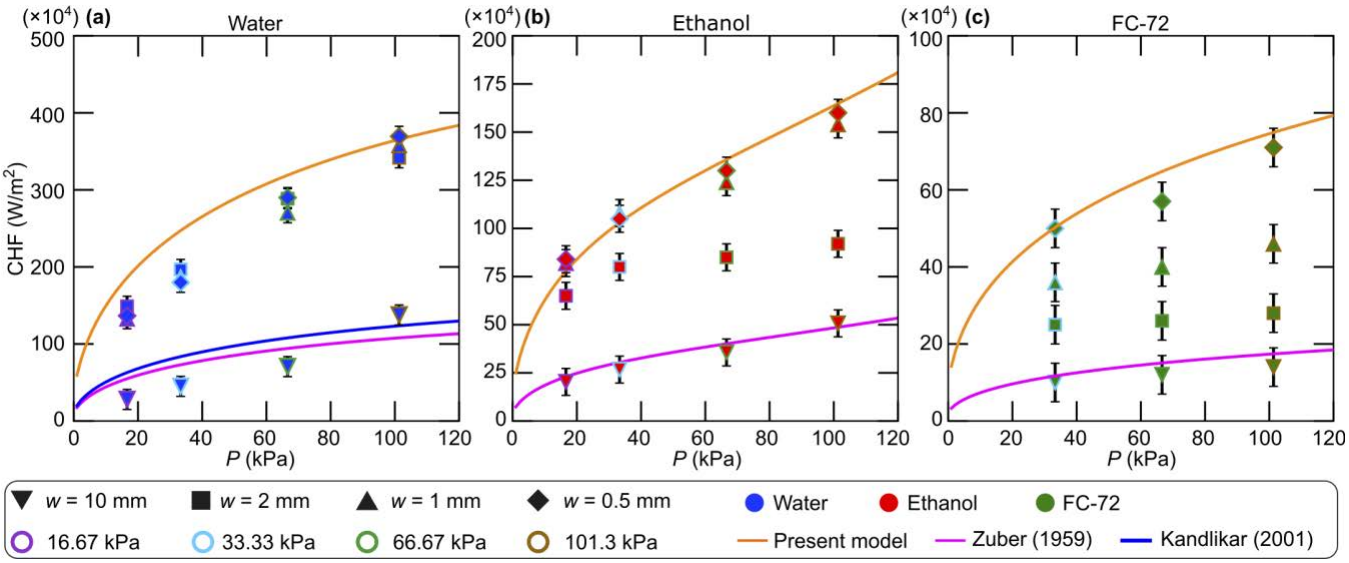

Fig. 8. Critical heat flux (CHF) on different surfaces for (**a**) water, (**b**) ethanol, and (**c**) FC-72. Inverted triangles represent surfaces with a width of 10 mm; squares, 2 mm; upright triangles, 1 mm; and diamonds, 0.5 mm. The error bars represent the uncertainty in recording the heat fluxes. The pink curves represent Zuber's prediction [20] for the respective liquid and surface configuration, orange curves represent the present model, while the blue curve represents Kandlikar's prediction [23].

the Cartesian axes, as indicated in Fig. 10. The momentum generated by evaporation, F_m, drives the radial expansion of the vapor pocket, counterbalanced by the surface tension force F_σ (illustrated by the blue arrow).

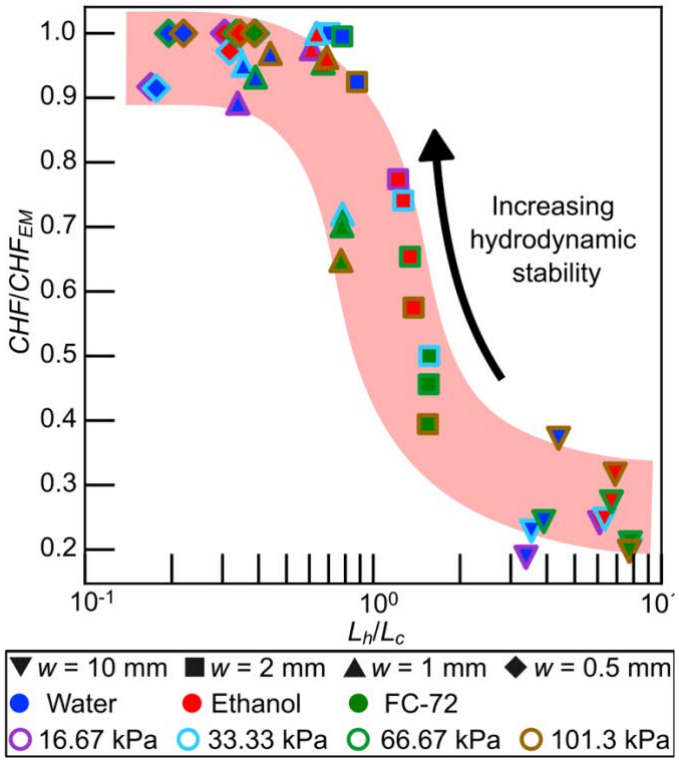

Fig. 9. CHF at all experimental conditions showing a universal trend demarcating regions governed by the hydrodynamic limit and the evaporation momentum limit.

Buoyancy also influences the bubble's interface, but its primary vertical direction has little impact on lateral expansion. To predict the CHF onset, we equate the horizontal force components, focusing on the x-direction. The analysis is limited to the bubble's left half; thus, the net horizontal evaporation momentum force, $F_{m,x}$, is oriented along the negative x-axis, opposite to Fig. 10 for visual simplicity. We compute $F_{m,x}$ as the integral of the x-component of vapor velocity V_x times the normal vapor velocity magnitude $\vec{V} \cdot \vec{n}$ across the area element $dA=r_b^2 \sin(\varphi)\,(d\theta \cdot d\varphi)$, representing a spherical surface segment.

The mass flux of evaporating vapor is given by $\dot{m} = q"A_i/h_{fg}$, where $q"$ is the incident heat flux contributing to the vapor generation, A_i $(= 4\pi r_b^2)$ is the area of influence responsible for supplying heat to the bubble, and h_{fg} is the latent heat of vaporization of the liquid. The mass flux can also be expressed as $\dot{m} = \rho_v A_b v$, where A_b is the surface area of the bubble/vapor pocket, and hence we can express the velocity of the vapor at the liquid-vapor interface $v = 4q"/(\rho_v h_{fg}(1 + \cos\beta))$.

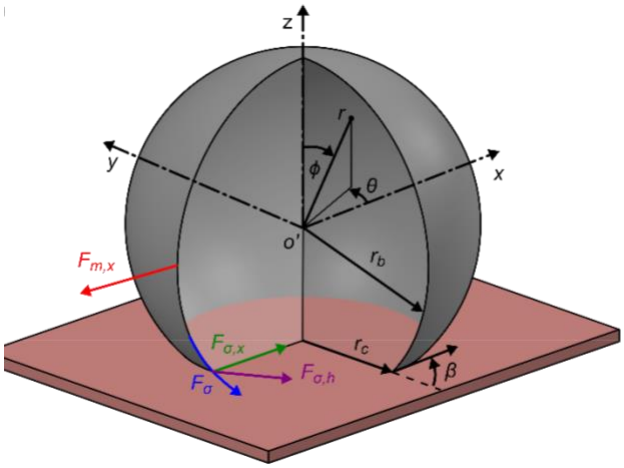

Fig. 10. CHF at all experimental conditions showing a universal trend demarcating regions governed by the hydrodynamic limit and the evaporation momentum limit.

The x-component of the velocity $v_x = v \cdot r\cos\theta\sin\emptyset$, hence, the horizontal x-component of the evaporation momentum force acting on the left half of the spherical cap is given by (4).

$$F_{m,x} = \left(\frac{q"}{h_{fg}}\right)^2 \frac{4r_b^2}{\rho_v(1+\cos\beta)^2}\left[(\pi-\beta)+\frac{1}{2}\sin 2\beta\right] \quad (4)$$

Next, the horizontal component of the surface tension force acting in the x-direction is evaluated. Considering the surface tension force as shown in Fig. 10, we see that F_σ (shown by the blue arrow) acts along the interface of the vapor pocket. $F_\sigma = \int dF_\sigma$, where $dF_\sigma(=\sigma\cdot dl)$ is the differential surface tension force and $dl(=r_b\cdot d\theta)$ is the differential line element on the liquid-vapor interface. Resolving this force into horizontal and vertical components, the horizontal component is given by $F_{\sigma,h} = F_\sigma\cos\beta$ (depicted by the purple arrow). The component of $F_{\sigma,h}$ in the x-direction is given by $F_{\sigma,x} = F_{\sigma,h}\cos\theta$. Similarly, the surface tension acting on the free surface of the left half of the bubble in the y-z plane can be estimated by integrating the differential surface tension element ($\sigma r_b\, d\alpha$) over the contour of the sphere in the y-z plane where α is the angle made by the differential element with the positive z axis and varies from $-(\pi-\beta)$ to $(\pi-\beta)$. The total surface tension force opposing the evaporation momentum force can accordingly be written as given in (5).

$$F_{\sigma,x} = 2\sigma r_b(\pi-\beta+\cos\beta) \quad (5)$$

CHF is triggered when the surface tension force is equal to the evaporation momentum force, and hence balancing (4) and (5) yields the expression for critical heat flux as given in (6)

$$CHF_{EM} = h_{fg}\rho_v^{\frac{1}{2}}[\sigma g(\rho_l-\rho_v)]^{\frac{1}{4}} \left\{\frac{(1+\cos\beta)}{[3\pi^2]^{\frac{1}{4}}}\left[\frac{\pi-\beta+\cos\beta}{\pi-\beta+\frac{\sin 2\beta}{2}}\right]^{\frac{1}{2}}\right\} \quad (6)$$

where the bubble diameter ($d_b = 2r_b$) is expressed as half the critical wavelength of Taylor instability, $d_b = \sqrt{3}\pi[\sigma/\Delta\rho g]^{1/2}$[20]. Here, $\Delta\rho(=\rho_l-\rho_v)$ is the difference in liquid and vapor densities of the fluid. Thermo-fluid properties for the tested liquids obtained from REFPROP, a Standard Reference Database distributed by the National Institute of Standards and Technology (NIST) [30] and dynamic contact angles of 80º for water and ethanol, and 72º for FC-72, extracted from experimental images, were used in (6) to estimate the theoretical CHF limit. The orange line in Fig. 6 represents (6) and closely matches all experimental data. Our experimental and theoretical analysis indicate that the evaporation momentum limit is fundamentally different from the hydrodynamic limit, in contrast to previous studies where the physics of evaporation momentum has been utilized to explain CHF on large surfaces. We suppose that the geometric considerations in previous estimates of the evaporation momentum limit, namely that of an infinitely long cylinder resting on the heater surface, result in CHF predictions close to the hydrodynamic limit. Lastly, we evaluate the contribution of the buoyancy force on the evaporation momentum limit and find that it is negligible.

Fig. 11 shows the percentage difference in two correlations for CHF, with and without consideration of buoyancy. The momentum force ($F_{m,x}$) is given in (4) and surface tension force ($F_{\sigma,x}$) is given by (5). The buoyancy force ($F_{b,x}$) is given by (7)

$$F_{b,x} = \frac{2}{3}\Delta\rho g r_b^4(\sin^3\beta) \quad (5)$$

where $\Delta\rho$ is the difference in density between the liquid and vapor, and g is the acceleration due to gravity. The two force balances considered are $F_{m,x} = F_{\sigma,x} + F_{b,x}$ and $F_{m,x} = F_{\sigma,x}$.

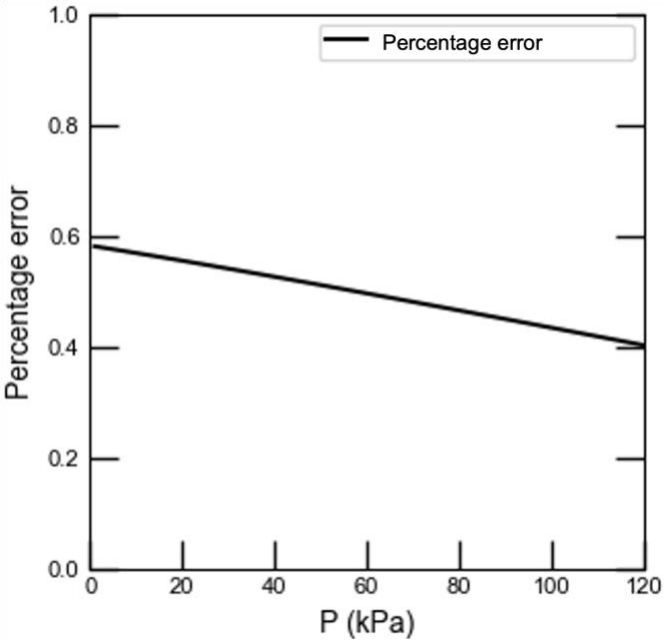

Fig. 11. Percentage error in the evaporation momentum model with and without the effect of buoyancy.

The difference in CHF obtained from the two force balances is ~ 0.5%, which clearly demonstrates the negligible effect of buoyancy. This effect is also experimentally verified as we only observe CHF_{EM} only below a *Bo* of 1, signifying the dominance of capillary effects over gravitational (or buoyancy) effects.

C. Implications for Immersion Cooling

Immersion cooling requires that the surface temperatures of electronics are maintained below the junction temperature to avoid failure. Fig. 12 illustrates the surface temperatures of different heaters during boiling of FC-72 at atmospheric pressure. The symbols correspond to identical data points in Fig. 8, signifying CHF values ranging from 16 to 72 W/cm^2. Fig. 12 demonstrates that a significant increase in CHF can be obtained ($4.5\times$) without any significant increase in surface superheat. This demonstrates that with appropriate flow structuring, immersion cooling with dielectrics such as FC-72 can be effective in maintaining chip junction temperatures below the acceptable value of 100 ℃. Future work will focus on development of surface topologies suitable for immersion cooling.

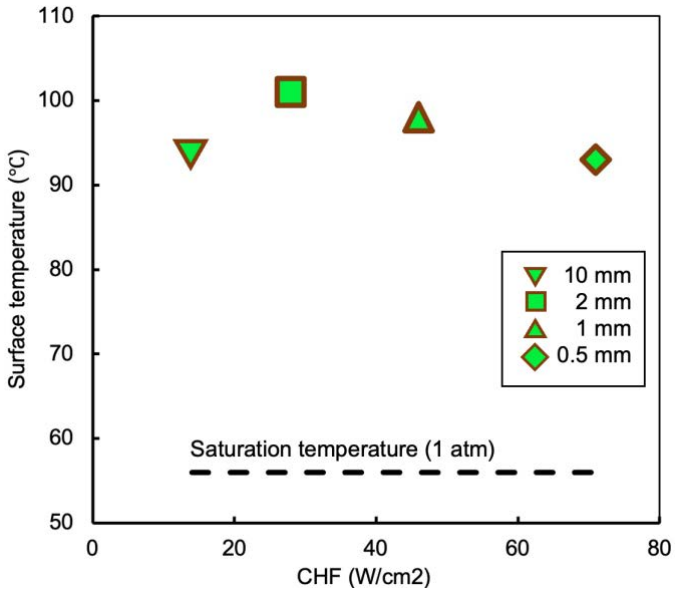

Fig. 12. Surface temperatures of FC-72 during CHF on different heaters at atmpospheric pressure. The black dashed line represents saturation temprature of FC-72 at 1 atm. The data corresponds to identical symbols in Fig. 6, signifying CHF values ranging from 16 to 72 W/cm^2.

IV. Conclusions

Our research on pool boiling spanned three distinct liquids: water, ethanol, and FC-72, chosen for their differing properties, which affect the capillary length (L_c). We varied the heater widths (w, or L_h) across a range relative to L_c and assessed 44 unique CHF values, exploring an order of magnitude in the L_h/L_c ratio. A diminishing L_h/L_c ratio resulted in more stable flow hydrodynamics and consequent CHF enhancement. At an L_h/L_c ratio nearing 1, CHF values surged, with ratios below ~1 entering the CHFEM regime. Specifically, water (L_c = 2.73 mm at 1 atm) showed CHF_{EM} on heaters of 2, 1, and 0.5 mm in width. Ethanol (L_c = 1.6 mm at 1 atm) reached the hydrodynamic limit on a 2-mm surface, while narrower heaters met the CHFEM limit. FC-72 (L_c = 0.72 mm at 1 atm) displayed CHF_{EM} only on the narrowest 0.5-mm heater. Plotting CHF normalized by CHF_{EM} against L_h/L_c revealed a universal increase as L_h/L_c decreased, with a steep rise at L_h/L_c ~1, clearly demonstrating the pivotal role of L_c. Additionally, our model incorporated a force balance on a spherical bubble, underscoring the necessity of spherical geometry for accurate CHF_{EM} predictions. This work could provide guidelines for development of surface topologies capable of dissipating high heat fluxes for use in immersion cooling.

Acknowledgment

S.R.T. thanks Mr. Sourabh Kakade for assistance with experiment setup.

References

[1] S. V. Garimella, L. T. Yeh, and T. Persoons, "Thermal management challenges in telecommunication systems and data centers," *IEEE Trans Compon Packaging Manuf Technol*, vol. 2, no. 8, pp. 1307–1316, 2012, doi: 10.1109/TCPMT.2012.2185797.

[2] N. Horner and I. Azevedo, "Power usage effectiveness in data centers: Overloaded and underachieving," 2016, doi: 10.1016/j.tej.2016.04.011.

[3] M. Dayarathna, Y. Wen, and R. Fan, "Data Center Energy Consumption Modeling: A Survey," *IEEE Communications Surveys & Tutorials*, vol. 18, no. 1, pp. 732–794, Jan. 2016, doi: 10.1109/COMST.2015.2481183.

[4] S. R. Tamvada and S. Moghaddam, "Data center energy efficiency enhancement using a two-phase heat sink with ultra-high heat transfer coefficient," Jul. 2022, doi: 10.48550/arxiv.2207.12508.

[5] S. R. Tamvada, M. Alipanah, and S. Moghaddam, "Membrane-Based Two Phase Heat Sinks for High Heat Flux Electronics and Lasers," *IEEE Trans Compon Packaging Manuf Technol*, vol. 11, no. 10, pp. 1734–1741, Oct. 2021, doi: 10.1109/TCPMT.2021.3115419.

[6] P. Birbarah *et al.*, "Water immersion cooling of high power density electronics," *Int J Heat Mass Transf*, vol. 147, p. 118918, Feb. 2020, doi: 10.1016/J.IJHEATMASSTRANSFER.2019.118918.

[7] V. P. Carey, *Liquid-Vapor Phase-Change Phenomena*. CRC Press, 2020. doi: 10.1201/9780429082221.

[8] S. NUKIYAMA, "The Maximum and Minimum Values of the Heat Q Transmitted from Metal to Boiling Water under Atmospheric Pressure," *Journal of the Society of Mechanical Engineers*, vol. 37, no. 206, pp. 367–374, 1934, doi: 10.1299/jsmemagazine.37.206_367.

[9] S. M. Kwark, R. Kumar, G. Moreno, J. Yoo, and S. M. You, "Pool boiling characteristics of low concentration nanofluids," *Int J Heat Mass Transf*, vol. 53, no. 5–6, pp. 972–981, Feb. 2010, doi: 10.1016/j.ijheatmasstransfer.2009.11.018.

[10] I. C. BANG, J. BUONGIORNO, L.-W. HU, and H. WANG, "Measurement of Key Pool Boiling Parameters in Nanofluids for Nuclear Applications," *Journal of Power and Energy Systems*, vol. 2, no. 1, pp. 340–351, 2008, doi: 10.1299/JPES.2.340.

[11] B. Shen *et al.*, "Enhanced pool boiling of ethanol on wettability-patterned surfaces," *Appl Therm Eng*, vol. 149, pp. 325–331, Feb. 2019, doi: 10.1016/j.applthermaleng.2018.12.049.

[12] C. H. Wang and V. K. Dhir, "Effect of surface wettability on active nucleation site density during pool boiling of water on a vertical surface," *J Heat Transfer*, vol. 115, no. 3, pp. 659–669, Aug. 1993, doi: 10.1115/1.2910737.

[13] H. O'Hanley *et al.*, "Separate effects of surface roughness, wettability, and porosity on the boiling critical heat flux," *Appl Phys Lett*, vol. 103, no. 2, p. 024102, Jul. 2013, doi: 10.1063/1.4813450.

[14] M. M. Rahman, E. Ölçeroğlu, and M. McCarthy, "Role of Wickability on the Critical Heat Flux of Structured Superhydrophilic Surfaces," *Langmuir*, vol. 30, no. 37, pp. 11225–11234, Sep. 2014, doi: 10.1021/la5030923.

[15] B. J. Jones, J. P. McHale, and S. V. Garimella, "The influence of surface roughness on nucleate pool boiling heat transfer," *J Heat Transfer*, vol. 131, no. 12, pp. 1–14, Dec. 2009, doi: 10.1115/1.3220144/415333.

[16] C. D. Henry and J. Kim, "A study of the effects of heater size, subcooling, and gravity level on pool boiling heat transfer," *Int J Heat Fluid Flow*, vol. 25, no. 2, pp. 262–273, Apr. 2004, doi: 10.1016/j.ijheatfluidflow.2003.11.019.

[17] S. M. Kwark, M. Amaya, R. Kumar, G. Moreno, and S. M. You, "Effects of pressure, orientation, and heater size on pool boiling of water with nanocoated heaters," *Int J Heat Mass Transf*, vol. 53, no. 23–24, pp. 5199–5208, Nov. 2010, doi: 10.1016/j.ijheatmasstransfer.2010.07.040.

[18] K. N. Rainey and S. M. You, "Effects of heater size and orientation on pool boiling heat transfer from microporous coated surfaces," *Int J Heat Mass Transf*, vol. 44, no. 14, pp. 2589–2599, Jun. 2001, doi: 10.1016/S0017-9310(00)00318-5.

[19] S. S. Kutateladze, "Hydrodynamic theory of changes in the boiling process under free convection conditions," *Омэ Тех Наук*, vol. 4, pp. 529–536, 1951.

[20] N. Zuber, "Hydrodynamic Aspects Of Boiling Heat Transfer (Thesis)," Oak Ridge, TN, Jun. 1959. doi: 10.2172/4175511.

[21] J. H. Lienhard and L. C. Witte, "AN HISTORICAL REVIEW OF THE HYDRODYNAMIC THEORY OF BOILING," 1985.

[22] K. Sefiane, D. Benielli, and A. Steinchen, "A new mechanism for pool boiling crisis, recoil instability and contact angle influence,"

Colloids Surf A Physicochem Eng Asp, vol. 142, no. 2–3, pp. 361–373, Dec. 1998, doi: 10.1016/S0927-7757(98)00614-1.

[23] S. G. Kandlikar, "A Theoretical Model to Predict Pool Boiling CHF Incorporating Effects of Contact Angle and Orientation," *J Heat Transfer*, vol. 123, no. 6, pp. 1071–1079, Dec. 2001, doi: 10.1115/1.1409265.

[24] G. I. Taylor, "The instability of liquid surfaces when accelerated in a direction perpendicular to their planes. I," *Proc R Soc Lond A Math Phys Sci*, vol. 201, no. 1065, pp. 192–196, Mar. 1950, doi: 10.1098/rspa.1950.0052.

[25] P. Helmholtz, "XLIII. On discontinuous movements of fluids," *https://doi.org/10.1080/14786446808640073*, vol. 36, no. 244, pp. 337–346, Nov. 2009, doi: 10.1080/14786446808640073.

[26] V. V. Yagov, "Is a crisis in pool boiling actually a hydrodynamic phenomenon?," *Int J Heat Mass Transf*, vol. 73, pp. 265–273, Jun. 2014, doi: 10.1016/j.ijheatmasstransfer.2014.01.076.

[27] S. Tamvada, D. Attinger, and S. Moghaddam, "On critical heat flux and its evaporation momentum and hydrodynamic limits," *Int J Heat Mass Transf*, vol. 203, p. 123837, Apr. 2023, doi: 10.1016/J.IJHEATMASSTRANSFER.2022.123837.

[28] J. Jung, S. J. Kim, and J. Kim, "Observations of the critical heat flux process during pool boiling of FC-72," *J Heat Transfer*, vol. 136, no. 4, Apr. 2014, doi: 10.1115/1.4025697/396457.

[29] A. Kalani and S. G. Kandlikar, "Enhanced pool boiling with ethanol at subatmospheric pressures for electronics cooling," *J Heat Transfer*, vol. 135, no. 11, Nov. 2013, doi: 10.1115/1.4024595.

[30] E. W. Lemmon, I. H. Bell, M. L. Huber, and M. O. McLinden, "NIST Standard Reference Database 23: Reference Fluid Thermodynamic and Transport Properties-REFPROP, Version 10.0, National Institute of Standards and Technology." 2018. doi: 10.18434/T4/1502528.